Xia, Z., Motagh, M., Li, T. (2022): Performance Analysis of Dihedral Corner Reflectors for Slope Movements: A Case Study From Aniangzhai Landslide in China. - IEEE Geoscience and Remote Sensing Letters, 19, 4515605.
https://doi.org/10.1109/LGRS.2022.3220649

Performance analysis of dihedral corner reflectors for slope movements: a case study from Aniangzhai landslide in China

Zhuge Xia, Mahdi Motagh, Tao Li

***Abstract*—Using SAR and InSAR technology, artificial corner reflectors (CR) are popular coherent targets for monitoring ground instability with sub-centimeter accuracy in non-urban areas. In this letter, we investigate the performance of a newly designed small dihedral corner reflector for monitoring post-failure creep at the Aniangzhai landslide in Danba County, China. The new double geometry CRs consist of two sets of semi-circular metal plates, each 30-40 cm in radius and perpendicular to each other. Six such CRs are installed for Corner Reflector Interferometric SAR (CR-InSAR) analysis using both TerraSAR-X (TSX) High-resolution Spotlight (HS) data and medium-resolution Sentinel-1 (S1) SAR images. The CRs are first identified in SAR images using a probability model by taking into three factors. These are (1) inverse of amplitude dispersion, (2) intensity increment after the installation, (3) an upper empirical bound derived from the ensemble average of pixel intensities in post-deployment SAR images. Experimental results show that the CRs improve the background intensity in TSX images by around 30 dB, with signal-to-clutter ratio (SCR) exceeding 25 dB. Furthermore, the radar cross-section (RCS) of CRs in both TSX and S1 images remains relatively stable, ranging from 15 dB to 23 dB, making them suitable for CR-InSAR analysis using double-difference phase observations.**

***Index Terms*—Satellite remote sensing, SAR Interferometry (InSAR), Corner reflector (CR), Radar cross-section (RCS), Signal-to-clutter ratio (SCR), TerraSAR-X (TSX), Sentinel-1 (S1).**

I. Introduction

ARTIFICIAL corner reflectors (CRs) are manufactured auxiliaries for synthetic aperture radar (SAR) and SAR Interferometry (InSAR) analysis, as they introduce coherent scatters with stable amplitude and phase information during radar acquisitions [1]. Deploying CRs as artificial coherent scatters is an alternative to increase the number of measurement points in multi-temporal InSAR analysis, especially when there is a risk of severe coherence loss between successive SAR image acquisitions in vegetated, semi-vegetated, or agricultural regions [2]. Due to their steady and robust echoes, traditional triangular corner reflectors (TCRs) with large dimensions, e.g., with an edge of 1 meter, have been proposed as an effective instrument for monitoring slope stability in vegetated mountainous areas [1]–[4].

Manuscript received XXX; revised XXX.

Zhuge Xia, and Mahdi Motagh are with Section of Remote Sensing and Geoinformatics, Department of Geodesy, GFZ German Research Centre for Geosciences, 14473 Potsdam, Germany.

Zhuge Xia, and Mahdi Motagh are with Institute for Photogrammetry and Geoinformation, Leibniz University Hannover, 30167 Hannover, Germany.

Tao Li is with GNSS Research Centre, Wuhan University, 430079 Wuhan, China.

The increase in the availability of high-resolution X-band SAR imagery by German TerraSAR-X (TSX) and the Italian CSMO-SkyMed (CSK) satellites has made the use of CRs more appealing, as such SAR systems could benefit from smaller CRs which can be installed in challenging environments with the advantage of having low cost, easy installation, and simple maintenance [5]. However, there is a limitation in using smaller CRs in that a reduction in power occurs due to the reduced size of reflectors that would limit their applicability for medium-resolution SAR images from missions like Sentinel-1 and ALOS-2 [5], [6]. It is worth noting that with regard to the design of CRs, no single design that could perform equally well for all of the currently operational SAR satellites [6]. Thus, a sensor-specific CR or a compromise solution for several sensors needs to be taken for operational monitoring.

In this study, we present the results of our experiment for using a newly designed dihedral corner reflector for monitoring post-failure creep at Aniangzhai landslides in China. The CRs have small dimensions (each 30-40 cm in radius), and are constructed with symmetrical geometry (Fig. 1), making them suitable for both ascending and descending SAR observations and broadening their application to those fields requiring the generation of 3D velocity maps from SAR data. Previous studies have shown that the primary deformation of the Aniangzhai landslide is along the north-west direction [7], which makes the landslide more sensitive to SAR observations from a descending track. Therefore, here we mainly focused on descending SAR images that have more sensitivity to slope motion in the study area. However, results from S1 ascending data are also presented for comparison purposes. Six CRs were deployed at different positions of landslides in November 2020 (Fig. 1a). Then through a research proposal with the German Aerospace Agency, we tasked High-resolution Spotlight (HS) data acquisition from a descending orbit between July 2020 and February 2022. We also analyzed Sentinel-1 (S1) ascending and descending data for a similar period to evaluate the performance of CRs for C-band SAR systems. In total, we exploited 51 TSX and 90 S1 images of the Aniangzhai landslide for this experiment.

This paper is organized as follows. Following this introduction, the design of the experiments and the selection strategy using a conditional probability model for CRs for different SAR sensors are introduced. Two important indices to evaluate the CRs, i.e., radar cross-section (RCS) and signal-to-clutter ratio (SCR), and the method of Corner Reflector

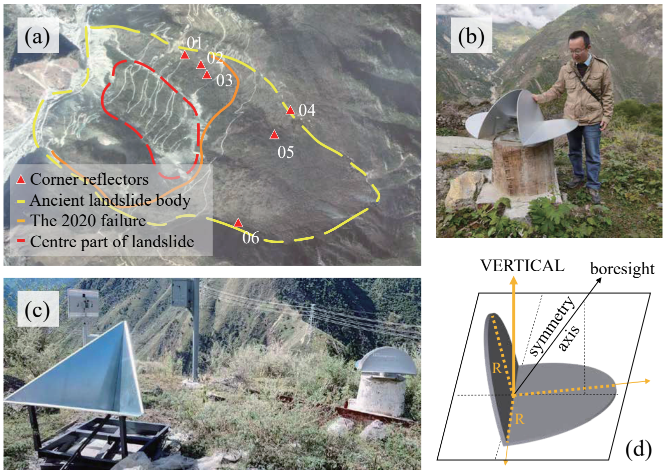

Fig. 1. (a) Study area and locations of tested CRs, specified by numbers 1-6. The background image is from a Skysat high-resolution optical image acquired in November 2020. The boundaries of different zones of the landslide body are presented [7]. (b) Field photo from a tested CR over Aniangzhai landslide. (c) Position relationship between CR03 and the newly arranged TCR as an unexpected interference. (d) The general schematic of constructed corner reflectors.

Interferometric SAR (CR-InSAR), are elaborated as well. Finally, the results of tested CRs are demonstrated, compared, and discussed in detail, followed by an overall conclusion of this study.

II. Experiments and Methodology

A. Experimental Design

CRs are usually composed of two or three electrically conducting surfaces to produce powerful radar echoes from areas with low effective RCS. Multiple reflections might precisely backscatter incoming electromagnetic waves in the same direction from which they come. As a result, even objects with small dimensions can produce mighty echoes. When CRs point directly along the boresight of a SAR antenna, the RCS of CRs could reach its maximum. Fig. 1d shows the schematic design and location of our CRs in the study area. They are composed of two sets of semi-circular metal plates positioned perpendicular to each other, so that they can be used for both ascending and descending high-resolution satellite imagery. These two sets are installed on a standard pillar, with the same inclination angle of 10° symmetrically. Among the six CRs, CR03 and CR04 have a radius of 40 cm, while the rest have a relatively smaller radius of 30 cm. The initial locations of the six CRs for the installation are measured with GPS.

B. Selection Strategy for CRs

In order to overcome difficulties such as biased GPS position or unpredictable interference with other scatterers (Fig. 1c), we propose a general selection strategy for identifying CRs in SAR images based on different properties and variations of power in pixels brought by the installation of CRs. The selection strategy is based on three different weighting factors. The first one is the inverse of amplitude dispersion index w_A, which represents the phase stability of CRs, with higher values being suggestive of more stability [8]. The second weighting factor w_I is the intensity increments of pixels after the installation, as theoretically we would expect the CRs to improve the lower clutter intensity in SAR images. The third weighting factor w_E is an upper empirical bound derived from the ensemble average of pixel intensities in sequential images after the deployment. This factor restricts selections of pixels other than CRs with stable and stronger signals that could come from, e.g., broken roads, buildings, and similar constructions on the landslide slope. Finally, after the derivation and normalization of all three weightings, a conditional probability model for every pixel is derived within the search window using

$$P_w = P(w_A) \cdot P(w_I|w_A) \cdot P(w_E|w_A, w_I) \tag{1}$$

According to the existing parameters, pixels with a more significant probability inside the search window are more likely to exhibit features similar to the tested CRs. In our experiment, this selection strategy helped properly identify and locate the tested CRs in both TSX and S1 images. Indeed, the method proposed here could also be exploited as a general strategy for other cases to identify similar targets with CR-like echoes. For example, when applied on other types of CRs, the only parameters that need to be changed in the above formulation are the time interval to estimate w_I and the empirical value for calculating w_E based on the properties of individual CRs.

C. Radar cross-section (RCS)

The projected area of a metal sphere scattering the same amount of energy in the same direction as the target is known as RCS [9], and its unit is often written in logarithmic form, i.e., dBm^2 or dBsm. RCS indicates the measure of the target's detectability [4], defined theoretically as

$$RCS = \frac{4\pi \cdot (A_e)^2}{\lambda^2} \tag{2}$$

where A_e is the projected area of the effective cross-section of CR, and λ is the wavelength, i.e., approximately 3.1 and 5.5 cm for TSX and S1 satellites, respectively. The maximum RCS of our tested CR with this specific design of geometry could be computed as

$$RCS_{max} = \frac{4\pi \cdot (\frac{\sqrt{2}}{2}\pi \cdot R^2)^2}{\lambda^2} = \frac{2\pi^3 \cdot R^4}{\lambda^2} \tag{3}$$

where R is the radius of the semi-circular metal plates. According to the equation (3), the maximum theoretical RCS of our CRs in TSX images is approximately 32.2 dB for the CRs with a 40 cm radius, and about 27.2 dB for 30 cm radius. As for S1 data, the CRs with a 40-cm and 30-cm radii have the maximum theoretical RCS values of around 27.2 dB and 22.2 dB, respectively.

Alternatively, RCS could also be measured directly from SAR images using the peak method in the spatial domain [10]

$$RCS_{measure} = E_{CR} \cdot A_{cell} \tag{4}$$

where E_{CR} is the intensity of CR, and A_{cell} is cell resolution. The measured RCS should be lower than the theoretical value due to the misalignment of the antenna.

D. Signal-to-Clutter Ratio (SCR)

SCR is another commonly used metric for target visibility in SAR images [11]. The targets such as CRs are needed to be much higher than the scattering level of the background. The SCR is defined as [11]

$$SCR = \frac{RCS_T}{\langle RCS_C \rangle} \tag{5}$$

where RCS_T represents the target RCS, and $\langle RCS_C \rangle$ is the ensemble average of clutter RCS neighboring the point target. For the conventional TCRs with strong power and cross-like signals in the SAR image, the clutter RCS is usually estimated with the average clutter intensity within the four clutter quadrants. However, in our study, the tested CRs were not strong enough to generate such cross-like signals due to small dimensions and differences in spatial resolution. Instead, only several concentrated pixels could be dominated and obtained. Thus, we derive the clutter RCS using an ensemble average within the search window neighboring tested CRs.

E. CR-InSAR Processing

Following identifying CRs, we exploit the CR-InSAR method for deformation analysis of the Aniangzhai landslide. CR-InSAR is a specific InSAR method applied for CRs [2]–[4]. It mainly exploits the information from double phase difference compared to a reference CR in different epochs

$$\Delta\phi_{ij} = (\phi_i^s - \phi_j^s) - (\phi_i^m - \phi_j^m) \tag{6}$$

where $\Delta\phi_{ij}$ represents the double phase difference of CRs i and j, the superscripts m and s are master and slave images. Then the wrapped phase obtained by double differencing needs to be unwrapped to estimate phase ambiguity. Here we used the least-squares ambiguity decorrelation adjustment (LAMBDA) method to estimate the absolute phase [12], and derive line-of-sight (LOS) motion based on linear and seasonal functional models. The atmospheric effects, i.e., tropospheric and ionospheric phase components, are neglected by the double-difference of phase observations considering the closing distance of deployed CRs [2], [3].

III. Results and Discussion

With the help of new methodology, we were able to identify our newly designed dihedral CRs correctly in both high resolution TerraSAR-X HS and medium resolution S1 data (see supporting material Figures S1-S4). The traditional ways to identify the conventional TCRs would be visual checking assisted by GPS coordinates as they would create intense echoes due to their large dimensions. However, this process does not work for our type of CR due to their small dimension and low energy. Moreover, due to the resampling of the CRs, the precise coordinate of CRs may not be the highest CR intensity peak. Our proposed strategy to identify small CRs has the following advantages: (1) It enables to identify CRs containing several concentrated pixels in SAR images, especially when CRs are located at the border of pixels. (2) It mitigates and reduces the influence of unpredictable interference from other scatterers with even stronger echoes in both high- and medium-resolution SAR images. (3) It can be adopted when the signals of tested CRs are not as strong as the conventional TCRs. (4) It can be utilized when the signals are influenced by low sensitivity and layover effect caused by satellite observation geometry. However, this selection strategy also has limitations in that it needs a priori information, e.g., the deployment time of CRs. With more a priori knowledge, a more reliable the estimation of the weighting factors could be obtained, leading to more accurate identification of CRs.

As revealed in Fig. 2, after selections of CRs in SAR images, we could obtain results of all the evaluation factors on the tested CRs. It is worth mentioning that TSX and S1 datasets are delivered in different types, i.e., the short complex and float complex format, respectively. Therefore, for a better comparison of two SAR data, the format of TSX images is first converted to the same as S1 data; then the calibrated intensity time series for two data are checked to ensure that the tested CRs exhibit identifiable scattering in SAR images. In order to illustrate the spatial distribution characteristics of radar intensity in this area, the radar intensity maps for the tested CRs are also displayed after their deployment (see Figures S5-S7 in supporting material).

Fig. 2a-2c show the time series of calibrated intensity on tested CRs in TSX and S1 data. In TSX images, the background intensities of the tested CRs are enhanced from approximately -15 dB to 15 dB after the deployment. For S1 images, however, this improvement is lower, i.e., by around 10 and 5 dB for the descending and ascending images, respectively. We also found that two CRs were missing by analyzing the results. CR04 could be observed initially after the deployment, but as of 2021, its intensity had decreased rapidly and was no longer visible in the search window. CR06 was completely missing in our analysis. Through the field investigation in late 2021, we found that the major reason for missing signals could be the skewed viewing orientations caused by man-made impediments, which were fixed during later fieldwork.

In general, we can say that the tested CRs work better in TSX images than in S1 images in improving the background clutter. This is mainly due to the great difference in spatial resolution between TSX and S1 SAR images, with the resolution of $0.9 \times 1.2\text{m}$ and $2.3 \times 14.0\text{m}$, respectively. Moreover, except for CR03 in S1 images, the intensity time series of CRs remains stable until the end of both SAR data. The calibrated intensity of CR03 shows a significant increase after June 2021 in S1 data. Checked by the fieldwork, we found that another group had set a new TCR with an edge of one meter very close to our CR03 (Fig. 1c, around 2$\sim$3 meters), which also appears in SAR data since June 2021. As a result, the intensity of CR03 interfered by this new TCR in S1 descending images, leading to an unusual signal rising (Fig. 2b). On the contrary, this interference was not dominant in TSX HS images due to their higher spatial resolution, enabling us to easily separate echoes from CR03 and its neighbouring CR (Fig. 2a), a task which was impossible to accomplish in medium-resolution S1 descending images. Besides, this TCR is descending-orbit orientated, so the results of S1 ascending data are not affected by the new TCR in the evaluation (Fig. 2c).

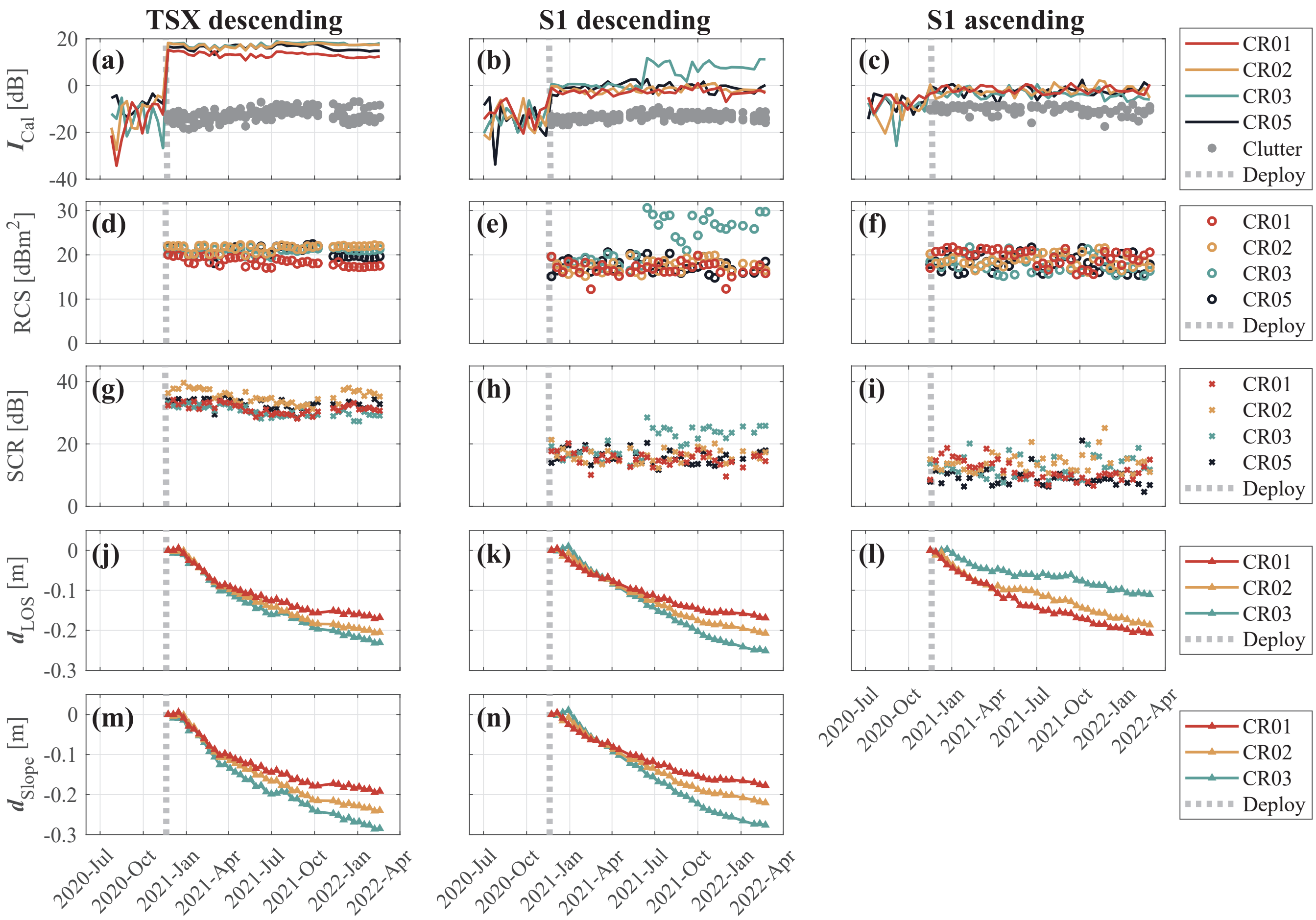

Fig. 2. Results of the tested CRs. (a)-(c) Time series of calibrated radar intensity. (d)-(f) Time series of the measured RCS values. (g)-(i) Time series of the measured SCR values. (j)-(l) LOS displacements estimated using CR-InSAR method. (m)-(n) Converted slope displacements on CRs. The left, middle and right columns are TSX descending, S1 descending, and S1 ascending datasets, respectively. The light gray dashed lines represent the deployment of the CRs.

Fig. 2d-2f demonstrate the time series of measured RCS on tested CRs in TSX and S1 images. Generally, we observe that the derived RCS values remain more or less stable for both TSX and S1 images, ranging from 15-23 dB; whilst the RCS of CRs in TSX images is approximately 5-10 dB higher than the values in S1 images. Compared to the theoretical RCS, it is not surprising that the derived RCS from SAR images could not reach the maximum analytical values expected, as the CRs are not optimally deployed for specific satellite orbits. Moreover, the CRs are not directed towards the boresight, too. Similar to the intensity analysis, the same rising feature of RCS for CR03 could be observed after June 2021 due to the influence of another TCR nearby.

Fig. 2g-2i reveal the time series of derived SCR for tested CRs in TSX and S1 images. Overall, SCR in TSX images exceeds 25 dB, suggesting the great potential for recognition between CRs and background clutter when using TSX images. On the contrary, SCR in S1 is lower, mainly around 15 dB and 10 dB in descending and ascending data. Although it is not as good as in TSX, the RCS of CRs in S1 images is still apparent compared to the clutter. This suggests that the tested CRs could be distinguished compared to the dark background coming from dense vegetation in this area. Taking into account SCR, the effective phase errors for TSX and S1 images are about 0.04 and 0.13 radians, respectively (see supporting material); while the effective displacement errors in the LOS direction are about 0.1 and 0.6 mm in X-band and C-band, respectively. Another interesting feature revealed in Fig. 2g is the drop of SCR values in TSX images since April and its increase in winter. This feature could possibly be linked to the increase in precipitation and growth in vegetation in the summer season that causes the drops of the SCR values [13].

Fig. 2j-2l reveal results from CR-InSAR analysis of CRs using TSX and S1 datasets with CR05 on the upper slope above the failure part of the landslide being selected as the reference CR. For the LOS displacements, the amounts of deformation from ascending and descending are different. For a better comparison, we further converted LOS displacements into slope displacements of the two descending SAR data. The movement of the landslide block may be controlled by a sliding surface that is approximately parallel to the surface of the slope [7]. Therefore, the average slope and aspect of the middle and lower parts of the landslide are exploited to calculate the scaling factors. Fig. 2m and 2n demonstrate the converted slope displacements from TSX and S1 descending datasets. Please note that the Aniangzhai landslide slope is facing to the west, which causes a layover effect in ascending orbit SAR data [14]. Moreover, it is not feasible to convert the S1 ascending data to slope direction, as this observation geometry has very low sensitivity to the landslide slope motion [14], [15]; during the process of calculation, the scaling factors for transformation from LOS direction to slope direction are within the interval of 0.19∼0.23, causing great artificial exaggeration and extreme values. Hence, the results derived from ascending orbit data are not as promising as the results from descending orbit.

As seen in Fig. 2m and 2n, for both TSX and S1 descending data, CR01-03 suggest similar kinematics of motion from the beginning until October 2021. After conversion into slope direction, the differences in magnitude of slope displacements between TSX and S1 data are found to be reduced compared to the differences in LOS displacements, i.e. from a few cm to 1 cm, especially for CR03. Until the end of October 2021, cumulative slope displacements of CR01-03 in TSX images are 17.8, 21.5, and 24.3 cm, respectively; in S1 images the displacements are 16.3, 19.4, and 24.0 cm, respectively. As of October 2021 we observe a distinct slowing-down of slope motion in both SAR images. The slowing down could be linked to the upslope loading from deposition of new material into the vacancies in landslide toe and foot areas [7], [16].

In a previous study, [5] successfully tested trihedral CRs with even smaller dimensions than ours containing an edge of around 14.5 cm, with their SCR of around 6 dB on average and improving the clutter intensity by around 6 dB. The small-scale CRs in [5] are specialized only to be used for high-resolution datasets such as TSX or CSK, and not for lower resolution datasets such as S1. Larger CRs would undoubtedly result in higher RCS and SCR values. However, the deployment and maintenance procedures would also be more difficult [4]. Our dihedral CR could act as a compromise solution among different CRs, which can be used for InSAR monitoring using both TSX and S1 SAR data at a relatively low cost with easy installation and maintenance.

IV. Conclusion

This study confirms that small dihedral corner reflectors designed within the framework of this experiment can reliably be used for deformation monitoring using CR-InSAR technique. An experimental study to assess post-failure creep at Aniangzhai landslide in China using both TerraSAR-X HS and S1 images showed that the background intensity in TSX images was enhanced by around 30 dB after CR installation, with SCR exceeding 25 dB. In comparison, the background intensity in S1 images was improved by only about 5-10 dB, with SCR of around 10-15 dB. In both TSX HS and S1 SAR images, the RCS of CRs remained rather consistent, ranging from 15 dB to 23 dB, making them appropriate for CR-InSAR analysis using the double-difference phase method. High-resolution SAR images have irreplaceable advantages in SAR and InSAR analysis due to the significant improvement in spatial resolution and shorter revisit times. Although our CRs were initially designed for X-band SAR systems, they illustrated sufficient SCR to be applied in S1 images for interferometric analysis, making them complementary to other traditional survey methods such as GPS or leveling. They can be installed quickly and easily at a relatively low cost in landslide regions, where ground-based measurements are lacking, for near real-time deformation monitoring and supplementing landslide hazard warning systems.

Acknowledgments

The authors acknowledged the German Space Agency (DLR) gratefully for providing the TerraSAR-X datasets, and the Copernicus programme for the free access to Sentinel-1 data. Z.X. is supported by China Scholarship Council (CSC) Grant #201908080048. This work is sponsored by the National Natural Science Foundation of China (No. 42074031).

References

[1] F. Bovenga, A. Refice, G. Pasquariello, D. O. Nitti, and R. Nutricato, “Corner reflectors and multi-temporal sar inteferometry for landslide monitoring,” in *SAR Image Analysis, Modeling, and Techniques XIV*, vol. 9243. International Society for Optics and Photonics, 2014, p. 92430I.

[2] X. Ye, H. Kaufmann, and X. Guo, “Landslide monitoring in the three gorges area using d-insar and corner reflectors,” *Photogrammetric Engineering and Remote Sensing*, vol. 70, no. 10, pp. 1167–1172, 2004.

[3] C. Froese, V. Poncos, R. Skirrow, M. Mansour, and D. Martin, “Characterizing complex deep seated landslide deformation using corner reflector insar (cr-insar): Little smoky landslide, alberta,” in *Proc. 4th Can. Conf. Geohazards*, 2008, pp. 1–4.

[4] X.-J. Shan, J.-Y. Yin, D.-L. Yu, C.-F. Li, J.-J. Zhao, and G.-F. Zhang, “Analysis of artificial corner reflector’s radar cross section: a physical optics perspective,” *Arabian Journal of Geosciences*, vol. 6, no. 8, pp. 2755–2765, 2013.

[5] P. Dheenathayalan, M. C. Cuenca, P. Hoogeboom, and R. F. Hanssen, “Small reflectors for ground motion monitoring with insar,” *IEEE Transactions on Geoscience and Remote Sensing*, vol. 55, no. 12, pp. 6703–6712, 2017.

[6] M. C. Garthwaite, “On the design of radar corner reflectors for deformation monitoring in multi-frequency insar,” *Remote Sensing*, vol. 9, no. 7, p. 648, 2017.

[7] Z. Xia, M. Motagh, T. Li, and S. Roessner, “The june 2020 aniangzhai landslide in sichuan province, southwest china: slope instability analysis from radar and optical satellite remote sensing data,” *Landslides*, vol. 19, no. 2, pp. 313–329, 2022.

[8] A. Ferretti, C. Prati, and F. Rocca, “Permanent scatterers in sar interferometry,” *IEEE Transactions on Geoscience and Remote Sensing*, vol. 39, no. 1, pp. 8–20, 2001.

[9] E. F. Knott, J. F. Schaeffer, and M. T. Tulley, *Radar Cross Section*. SciTech Publishing, 2004.

[10] I. Ulander, “Accuracy of using point targets for sar calibration,” *IEEE Transactions on Aerospace and Electronic Systems*, vol. 27, no. 1, pp. 139–148, 1991.

[11] A. Freeman, “Sar calibration: An overview,” *IEEE Transactions on Geoscience and Remote Sensing*, vol. 30, no. 6, pp. 1107–1121, 1992.

[12] B. M. Kampes and R. F. Hanssen, “Ambiguity resolution for permanent scatterer interferometry,” *IEEE Transactions on Geoscience and Remote Sensing*, vol. 42, no. 11, pp. 2446–2453, 2004.

[13] T. Kozu, T. Kawanishi, H. Kuroiwa, M. Kojima, K. Oikawa, H. Kumagai, K. Okamoto, M. Okumura, H. Nakatsuka, and K. Nishikawa, “Development of precipitation radar onboard the tropical rainfall measuring mission (trmm) satellite,” *IEEE Transactions on Geoscience and Remote Sensing*, vol. 39, no. 1, pp. 102–116, 2001.

[14] M. Haghshenas Haghighi and M. Motagh, “Assessment of ground surface displacement in taihape landslide, new zealand, with c-and x-band sar interferometry,” *New Zealand Journal of Geology and Geophysics*, vol. 59, no. 1, pp. 136–146, 2016.

[15] M. Motagh, H.-U. Wetzel, S. Roessner, and H. Kaufmann, “A terrasar-x insar study of landslides in southern kyrgyzstan, central asia,” *Remote Sensing Letters*, vol. 4, no. 7, pp. 657–666, 2013.

[16] P. Lacroix, A. L. Handwerger, and G. Bièvre, “Life and death of slow-moving landslides,” *Nature Reviews Earth & Environment*, vol. 1, no. 8, pp. 404–419, 2020.